**Title:**

# Hand and face somatotopy shown using MRI-safe vibrotactile stimulation with a novel Soft Pneumatic Actuator (SPA)-Skin interface

**Authors:**

Sanne Kikkert[1,2], Harshal A. Sonar[3], Patrick Freund[2], Jamie Paik[3], Nicole Wenderoth[1]

*[1]Neural Control of Movement Laboratory, Department of Health Sciences and Technology, ETH Zürich, Zürich, Switzerland.*

*[2]Spinal Cord Injury Center Balgrist, University Hospital Zürich, University of Zürich, Zürich, Switzerland.*

*[3]Reconfigurable Robotics Lab, EPFL, Lausanne, Switzerland.*

**Corresponding author:**

sanne.kikkert@hest.ethz.ch

**Abstract:**

The exact somatotopy of the human facial representation in the primary somatosensory cortex (S1) remains debated. One reason that progress has been hampered is due the methodological challenge of how to apply automated vibrotactile stimuli to face areas in a manner that is: 1) reliable despite different curvature depending on the face location; and 2) MR-compatible and free of MR-interference artefacts when applied in the MR head-coil. Here we overcame this challenge by using soft pneumatic actuator (SPA) technology. SPAs are made of a soft silicon material and can be in- or deflated by means of airflow, have a small diameter, and are flexible in structure, enabling good skin contact even on curved body surfaces (as on the face). Here,

we aimed to provide a methodological advance by providing automated tactile vibration stimulation inside the head-coil of the MRI. As a sanity check, we first mapped the well-characterised S1 finger layout using this novel device. We found that tactile stimulation of the fingers elicited characteristic somatotopic finger activations in S1, validating the use of our SPA-setup to map somatotopic representations. Ultimately, we used the device to automatically and systematically deliver somatosensory stimulation to different face locations. We found that the forehead representation was least distance from the representation of the hand. Within the face representation, we found that the lip representation is most distant from the forehead representation, with the chin represented in between. Together our results show that, by providing vibrotactile stimulation using the SPA-technology, we are able to reveal clear somatotopic representational patterns.

**Keywords:**

Somatosensory, vibrotactile technology, fMRI, face, hand, soft pneumatic actuators

## Introduction

Over the past decades, somatotopic mapping had provided us with an increasingly better understanding of our body representations. However, providing tactile stimulation in an MR environment remains challenging. Experimenters commonly use an active movement paradigm (Kolasinski et al., 2016; Schellekens et al., 2018; Zeharia et al., 2015) or manual stroking of body parts (Martuzzi et al., 2014; Sanders et al., 2019; Van Der Zwaag et al., 2015) to probe somatotopic representations. While manual stroking may provide adequate somatosensory cortical signals and movement paradigms may better reflect real-life situations, such paradigms induce participant and experimenter dependent spatiotemporal variance affecting the statistical images. Indeed, the intensity, timing, and body part coverage of active paradigms and manual stimulations may not be consistent and precise. Furthermore, a somatotopic mapping that can distinguish between body parts that are not able to move independently (e.g., certain parts of the face, toes) is impossible using an active movement paradigm. Similarly, manual stroking of different body parts simultaneously, of the face when using a narrow head coil, or of the body when using a full body coil, is challenging. The usage of mechanical vibrotactile devices provides an opportunity to overcome these limitations. However, common vibrotactile elements contain metals or electrical circuits that are mostly not compatible with the MR environment (Yu and Riener, 2006). Stimulating body parts in (or close to) the MR head coil is especially technically demanding given the narrow geometry of the head coil and the safety constraints and imaging artefacts induced by small metal components.

In the past decades, a variety of MR-compatible vibrotactile devices have been developed. Commercially available piezoelectric and piezoceramic devices, for example, are able to deliver vibrotactile stimulation at high frequency ranges at a chosen amplitude. However, these devices mostly still contain some metal components and lead electrical wires

inside the scanner (Puckett et al., 2017; Sanchez-Panchuelo et al., 2010). The electrical wires may be heated by RF pulses if not shielded properly. While this active shielding is sufficient when the stimulators are placed away from the head coil (e.g., on the fingers), they can (in certain cases) induce unwanted signal interference and safety issues when placed closer to, or inside, the MR head coil. Pneumatically driven or air puff devices circumvent issues of such electromagnetic interference and can be made of plastic tubes and MR compatible materials.

The pneumatic devices that have been developed for safe delivery of tactile stimulation to multiple stimulation sites inside the MR head coil are however limited. Indeed, most pneumatically driven devices have been built for providing stimulation to e.g., the fingers or other body parts further away from the head coil (Gallasch et al., 2010; Golaszewski et al., 2002). The Dodecapus was amongst the first pneumatically driven devices build to apply automated tactile stimulation to a range of face locations. Its control system is placed outside the MR environment and air puffs are delivered to specified parts of the face (or other body parts) through long plastic tubes (Huang and Sereno, 2007). The device was extended to deliver punctate tactile stimuli to the face using Von Frey-filaments with a high spatiotemporal accuracy (Dresel et al., 2008). However, in these setups stimulation could only be applied to parts of the face that are exposed (i.e., that are not covered by the head coil). Later, flexible plastic tubes were attached to a facial mask (custom modelled for each subject) to deliver air puffs to different locations of the face (Chen et al., 2017; Huang et al., 2017). With this new implementation the authors were able to reach areas of the face that are covered by the head coil, allowing for a more complete picture of face somatotopy. However, this face mask may not fit in head coils with more narrow geometry and when using participants with larger head sizes. Furthermore, providing air puffs close to the mouth, nose, or eyes may not be comfortable for participants. More recently, the GALILEO Somatosensory™ was developed. This device can provide tactile stimulation through pressure dynamics in individual stimulators with high

spatiotemporal control (Custead et al., 2017). While this device is very promising and allows the study of stimulation velocity, the stimulators are 6mm in height and may not fit in head coils with very narrow geometry, especially in situations/locations where the spacing between the head coil and parts of the face only persists of a few millimetres. Furthermore, it may not be easy to attach the stimulators to highly curved body surfaces and the device is rather expensive.

An optimal vibrotactile device for MRI usage would be pneumatic such that all components inside the MR environment would consist of MR-safe materials, ensuring that it does not induce any MR interference artefacts and is safe to be placed on the skin, even inside the MR head coil. The control device containing the necessary electronics should be placed outside the MR environment. Further, it should allow good control over vibration frequency and amplitude, enabling both sub- and suprathreshold vibrotactile stimulation. The stimulators itself should be flexible in nature, such that they can be placed on skin surfaces with different curvature. The stimulator should further be small to provide focal stimulation, and narrow, such that it can easily be placed in narrow head coils that are typical for ultra-high field imaging. Lastly, the stimulator should be portable and cost-efficient.

An accurate and detailed somatotopic understanding of the human body will improve our understanding of the somatosensory system and aid our investigation of somatosensory remapping after peripheral body and spinal cord injuries (Corbetta et al., 2002; Flor et al., 1995; Jutzeler et al., 2015; Makin et al., 2015; Moxon et al., 2014; Root et al., 2021). While the gross representation of body parts and fingers in S1 is agreeable across studies, results on the exact somatotopic mapping of the face have been mixed. Contrasting work reports both an inverted (Servos et al., 1999; Yang et al., 1993) and upright somatotopic face representation (Huang and Sereno, 2007; Penfield and Rasmussen, 1950; Root et al., 2021; Roux et al., 2018; Sato et al., 2005; Schwartz et al., 2004). Yet other studies were unable to find clear inverted or upright

115 representations of face and rather reported more mixed face representations following an
116 'onion skin model' where the nose was represented more inferior in S1 than stimulations on
117 the lower jaw or above the eye (DaSilva et al., 2002; Moulton et al., 2009). To detail the full
118 somatotopic layout of the face an automated face stimulation paradigm and both univariate
119 analysis and multivariate analysis methods that are sensitive to representational overlaps (i.e.,
120 representational similarity analysis) are needed.

121 In this study, we developed a novel tactile stimulation device capable of providing focal
122 and suprathreshold vibrotactile stimulation to the face and other parts of the body. We used
123 soft pneumatic actuator (SPA) skin technology that, unlike common vibrotactile elements, does
124 not contain metals and still provide excellent control over actuation frequencies (Harshal A.
125 Sonar et al., 2019; Sonar and Paik, 2016). SPAs are made of a soft MR-safe silicon material
126 (Dragon Skin 30®, Smooth On Inc., USA) and can be in- or deflated by means of airflow.
127 SPAs have a small (1.4cm) diameter, are soft and flexible in structure, enabling good skin
128 contact even on curved body surfaces (as on the face). Furthermore, the low profile design of
129 the SPA-skin (under 1mm) allows for usage in the narrow geometry of the MR head coil and
130 in narrow bores that are typical for ultra-high field MRI environments. We demonstrated the
131 feasibility of using the SPA-skin-setup for somatotopic mapping in an fMRI study. We
132 hypothesized that tactile stimulation using the SPA-skin would yield robust localised
133 activations in somatosensory areas. We further hypothesized that tactile stimuli of the fingers
134 would elicit characteristic somatotopic finger activations in the primary somatosensory cortex.
135 Lastly, we investigated the somatotopic layout of face, using the device to automatically and
136 systematically deliver somatosensory stimulation inside the head coil.

137 # Materials and methods

138 **Participants**

139 Seventeen healthy participants (mean age ± s.e.m. = 37.5 ± 4.3; 7 females; 2 left-handers)
140 participated in this study. Ethical approval was granted by the Kantonale Ethikkommission
141 Zürich (EK-2018-00937) and written informed consent was obtained prior to study onset. This
142 study is registered on clinicaltrials.gov under the number NCT03772548. As our fingers
143 stimulation experiment was meant as a mere validation of the device and was expected to reveal
144 convincing data in a limited number of participants, we only tested 8 participants for this
145 feasibility aspect of the study. All participants were tested for face somatotopy.

146

147 **SPA-skin stimulator design**

148 Soft robotics emerged as a new field in robotics over a past decade and has been growing across
149 the applications in medical technologies, personal care, environmental monitoring and
150 entertainment (Bauer et al., 2014; Gibson, 2018; Hawkes et al., 2017; Jafari et al., 2016;
151 Polygerinos et al., 2017). Soft robotics tackles the interactivity and wearability challenges
152 posed to traditional rigid body robotic systems by using soft material based sensors and
153 actuators to replace the traditional sensors and motors. These soft materials enable an
154 inherently safe and mechanically compliant feedback to the environment including a human
155 wearer (Polygerinos et al., 2017, 2015; Pons, 2008; Robertson and Paik, 2017). Wearability of
156 soft technology can further be used to improve traditional haptic communication devices that
157 currently only provide limited wearability due to their bulky and rigid-form factors (Cholewiak
158 and Collins, 2003; Jones, 2011; Yun et al., 2017). Present haptic feedback devices mainly rely
159 on motors and components driven using electromagnetic eccentric mass or piezoelectric motors
160 that have limited wearability due to their bulky rigid mechanisms and cannot be used in

environments prone to electromagnetic interference like the MRI environment (Alahakone and Senanayake, 2009; Cholewiak and Collins, 2003; “Smart Tactor Development Kit,” 2021).

We developed a novel soft skin like interface (Figure 1): i.e., a soft pneumatic actuator (SPA)-skin that can be driven using pneumatics and is capable of generating plethora of actuation in the range of 10-100 Hz and can be complemented by integrated sensors (Sonar et al., 2019; Sonar et al., 2019; Sonar and Paik, 2016). The SPA-skin is fabricated using silicone material (Dragon Skin 30, Smooth-On Inc., USA) that has similar stiffness as human skin and provides optimal comfort, as is necessary for long duration fMRI studies (Figure 2). The actuator layer, i.e., the SPA, consists of an elastomeric membrane that can be pneumatically inflated with a pressure input (Sonar and Paik, 2016; see Figure 2B). This actuator is fabricated with three thin layers with a total thickness of 500-1000 μm: a middle flexible mask layer (50μm) to define the actuator’s shape that is sandwiched between two silicone layers. The masking layer is laser cut to obtain the desired shape and is then laminated onto the bottom silicone layer to be encapsulated by a thin top silicone layer. The polypropylene mask adheres to the bottom silicone and ensures that, upon inflation, deformation occurs in the top membrane. It is important to ensure a proper grounding with the skin and attaching the SPA-skin properly at given location without obstructing the inlet pneumatic flow lines.

For any robotic system, sensor feedback plays an important role to ensure an accurate control and understanding of the surrounding environment. The traditionally available pressure or force sensors, needed for providing coherent tactile feedback, work well but like rigid tactile stimulators, these are also limited in their application when they need to be worn by humans, as they often lack the much needed compliance with human body. We have hence developed and integrated possibilities of sensing layers in the SPA-skin that provide localised measurement of interactive forces by virtue of different sensing technologies including active piezo charge sensing (Sonar and Paik, 2016) or passive methods like resistive strain sensor (

186 Sonar et al., 2019) and soft capacitive skin (Sonar et al., 2018). The sensing layer and the SPA-
187 skin design process tackle this challenge using a finite element based simulation (Agarwal et
188 al., 2017; Moseley et al., 2016) and closed loop feedback control through the sensing layer.
189 This ensures an accurate tactile stimulation even under variable loading conditions or
190 manufacturing variabilities (Sonar and Paik, 2016).

191 For the fMRI compliant tactile stimulator application we chose a ring shaped SPA
192 design (with a 1.4cm diameter and 2mm inlet tube channel) to maximize the application area
193 on skin while minimizing the volume of air being transferred through the long tubing that helps
194 improving the maximum actuation frequency or bandwidth. The in-house developed setup
195 independently controlled 8 channels that extended to different SPA-skins. The need for long
196 tubing (5m to 6m) limited the amount of air being pushed to the actuators during inflation and
197 then back during the deflation cycle. A careful system design was therefore carried out for each
198 component of the pneumatic supply system (PSS) to achieve maximum bandwidth at 6m tube
199 length and maintaining expected functionality of SPAs at less than 80kPa, as discussed in detail
200 in (Joshi et al., 2021; Joshi and Paik, 2021). This allowed us to stretch the actuation bandwidth
201 up to 15Hz in the current setup. When attempting to reach a bandwidth of 30Hz, we were still
202 able to measure 0.5N of force at 30Hz, which is largely above the perception threshold for the
203 face and fingers.

204 The SPA-skin was pneumatically controlled through an in-house developed control
205 circuit that was interfaced through a serial communication to the stimulus computer (see Figure
206 1). The pneumatic controller was composed of the following components: a stimulus computer,
207 a portable air compressor, a portable pneumatic control circuit module, and corresponding
208 pneumatic tubes. An air compressor (Implotex, Germany) provided airflow to a pressure
209 regulator (ITV1050, SMC Corp.,USA) that was controlled by the microcontroller in the control
210 circuit. The stimulation intensity could be adjusted using a single pressure regulator and an

array of high-speed solenoid valves which were driven through high-power MOSFET switches and stimulus from the micro-controller.

A portable pneumatic supply line, AC power supply and USB cable for serial communication enabled the primary extension of the controller setup to be placed just outside the RF shielding walls of the fMRI scanner. A 50mm diameter hole in the wall then carried the 5-6m long and 4mm thick tubes to the SPAs that were places on the face or the fingers. Once connected in this fashion, the system acted as a plug-n-play device that can be easily controlled via the stimulus computer using simple serial commands to turn a given channel on or off at a given frequency. The pressure regulator could be manipulated through the stimulus computer and the working pressure of the pneumatic system could be read in realtime. The build-in limitation of 100kPa operational pressure ensures a delamination free operation of the SPA-skin.

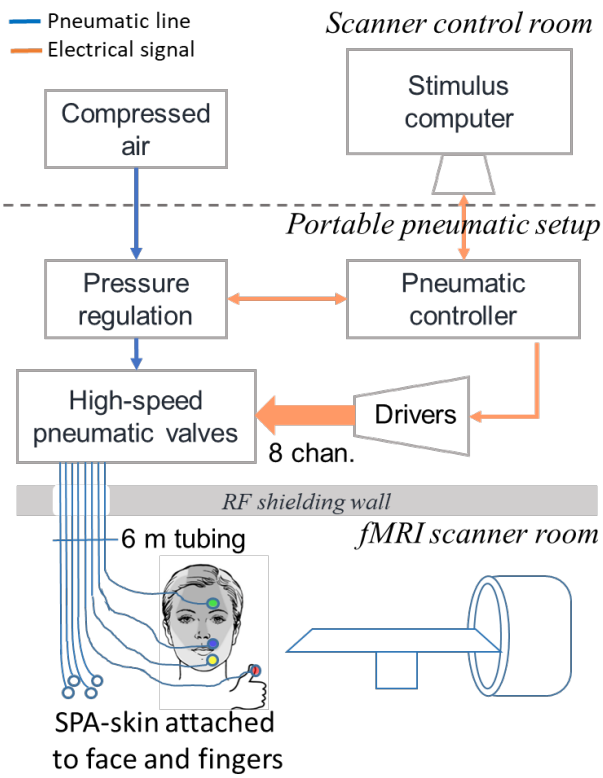


**Figure 1: Schematic illustration of the SPA setup.** The pneumatic controller was composed of the following components: a stimulus computer, a portable air compressor, a portable pneumatic setup, and pneumatic tubes. Stimulation intensity and frequency could be controlled using a stimulus controlled places in the scanner control room. An air compressor (Implotex, Germany) places in the scanner control room provided airflow to a pressure regulator that was controlled by the microcontroller in the portable pneumatic setup. The stimulation intensity could be adjusted using the pressure regulator and an array of high-speed pneumatic valves which were driven through high-power MOSFET switches and inputs from the micro-controller. A 50mm diameter hole in the RF shielding wall then carried the 5-6m long and 4mm thick tubes to the SPAs that were places on the face or the fingers in the fMRI scanner room.

## Experimental paradigm

SPAs were attached to the forehead (~1cm above the eyebrow), above the upper lip, and on the chin (see Figure 2A). These sites were chosen to ensure that an SPA was placed on each of the trigeminal nerves' innervated skin areas. Care was taken to not place SPAs on skin areas that are on the border of trigeminal nerve innervations. To ensure good grounding of the SPAs on

240 the face, we placed in-house 3D printed plates on top of the SPAs and used a custom-made
241 fabric face mask to apply light pressure to the SPAs (see Figure 2B). Five further SPAs were
242 attached to the fingertips of the left hand using adhesive tape.

243 Participants viewed a visual display positioned at the head of the scanner bore through
244 a mirror mounted on the head coil. Participants 1-9 were presented with horizontally (for the
245 finger stimulation runs) or vertically (for the face stimulation runs) aligned white circles,
246 corresponding to the different stimulation locations. To cue the participant which location
247 would be stimulated, the circle corresponding to this location turned red 0.8sec prior to
248 stimulation onset and remained red until stimulation offset. Participants 10-17 were cued with
249 the words "Forehead", "Lips", "Chin", and "Thumb" presented in white centred on a black
250 screen. To cue the participant which location would be stimulated, the text cue appeared on the
251 screen 0.8sec prior to stimulation onset and remained on the screen until stimulation offset.

252 Participants were instructed to attend to the highlighted stimulation location as long as
253 the cue was presented on the screen. Stimulation was presented for 8s at 8Hz with 900ms bursts
254 of stimulation 'on' periods followed by a 100ms 'off' period to minimise peripheral adaptation.
255 To ensure stable attention during the fMRI runs, stimulations were interrupted in a small
256 percentage of the stimulation blocks (10-20% of trails per run). In these interrupted stimulation
257 trials, stimulation was provided for 4s, after which a 2s silent period was introduced, following
258 by another 2s of stimulation. Care was taken to ensure that the interrupted stimulation trials
259 were equally distributed across the stimulation locations within each run. Participants were
260 instructed to count the number of interrupted stimulation trials and verbally report this at the
261 end of each run.

262 Since a stronger sensation is expected to lead to a stronger BOLD response, we aimed
263 to match the sensation intensity across stimulation locations prior to the fMRI runs. A
264 stimulation intensity matching task was carried out for the face and finger stimulation runs

separately. First, participants were asked to set the optimal stimulation intensity for a reference location. The forehead location was chosen as a reference for the face stimulation runs, and the little finger was chosen as the reference location for the finger stimulation runs. We chose these stimulation locations as references, since they are innervated by least mechanoreceptors and are therefore likely to be least sensitive (Corniani and Saal, 2020). Participants were instructed that an optimal stimulation intensity would be as strong as possible while remaining focal (i.e., no spread to skin locations not directly underneath the stimulator), comfortable, and stable over the 8s stimulation period (i.e., minimal peripheral adaptation). Participants were asked to respond by means of a button box whether the intensity should be decreased, increased, or should not change. Based on the participants' response the air pressure provided to the SPAs was decreased or increased in steps of 5 kPa (leading to a lower or higher stimulation intensity, respectively) or remained stable. If the participant responded twice in a row that the stimulation intensity should not be changed, the stimulation pressure for the reference location was set at this level for all fMRI tasks. Since the SPAs become fragile when using an air pressure exceeding 80 kPa, this was the maximum pressure setting that could be chosen by participants. The minimum air pressure provided was set at 20 kPa above atmospheric pressure. Once the optimal stimulation intensity was chosen for the reference location, participants were asked to match the stimulation intensity for the other stimulation locations to the stimulation intensity of the reference location. To enable this matching, participants were initially given an 8.8s stimulation trial for the reference location, immediately followed by a stimulation trial of one of the other stimulation locations. Participants were instructed to change the stimulation intensity of the 2$^{nd}$ location to match the stimulation intensity of the reference location as closely as possible. For the face stimulation runs, participants were instructed to match the stimulation intensity of the lips, chin, and thumb to the reference forehead stimulation intensity. For the face stimulation runs, participants were instructed to match the stimulation intensity of

the thumb, index, middle, and ring finger to the reference little finger stimulation intensity. As before, if the participant responded twice that the stimulation intensity should not be changed, the stimulation pressure for this stimulation location was set at this level for all fMRI tasks.

Instructions and stimulations were delivered using Psychtoolbox (v3) implemented in Matlab (v2014b). Matlab then communicated with the Arduino board implemented in the SPA controller set-up via a serial port over a proprietary protocol. Head motion was minimized using over-ear MRI-safe headphones or padded cushions.

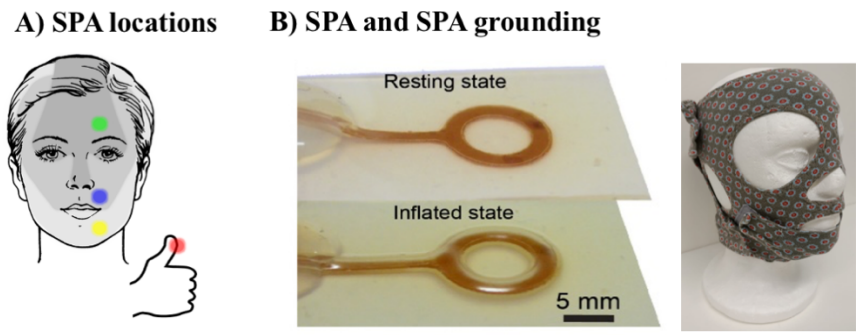


**Figure 2: SPA locations and grounding on the face.** A) SPAs were attached to the forehead, upper lip, chin, and thumb. We either tested the right or the left side of the face and the right of the left thumb. Shaded areas on the face indicate the skin areas innervated by different branches of the trigeminal nerve. B) SPAs were grounded to the face using a custom made fabric mask.

## Fingers stimulation runs

The finger stimulation blocked design consisted of 6 conditions: Stimulation conditions for each of the five fingers of the left hand and a rest (no stimulation) condition. The visual cue during the finger stimulation blocks was as described above and presentation of the word "Rest" indicated the rest condition. Each of these 6 conditions had a block duration of 8.8s and was repeated 5 times per run in a counterbalanced order. Each run comprised a different block order and had a duration of 4min and 39.4s. We acquired 4 blocked design runs, with a total duration of 18min and 37.6s.

312

313 **Face stimulation runs**

314 All face stimulation runs also involved stimulation of the forehead, lips, chin, and thumb. 14
315 participants were stimulated on the left side of their face and the left thumb. 3 participants were
316 stimulated on the right side of the face and their right thumb. We included thumb stimulation
317 in these runs as the thumb representation borders the face area in S1 (Kikkert et al., 2021, 2016;
318 Kolasinski et al., 2016; Penfield and Rasmussen, 1950; Roux et al., 2018). To uncover face
319 somatotopy we used a blocked design consisting of 5 conditions: Stimulation conditions for
320 each of the three face locations and for the thumb, as well as a rest (no stimulation) condition.
321 The visual cue during the face stimulation blocks were as described above and presentation of
322 the word "Rest" indicated the rest condition. Each of these 5 conditions had a block duration
323 of 8.8s and was repeated 8 times per run in a counterbalanced order. Each run comprised a
324 different block order and had a duration of 6min and 7.4s. We acquired 4 blocked design runs,
325 with a total duration of 24min and 29.6s.

326

327 **MRI acquisition**

328 MRI data was acquired using a Philips 3 tesla Ingenia system (Best, The Netherlands). Data of
329 participants 1-9 was collected using a 32-channel head coil and data of participants 10-18 was
330 collected using a 15-channel head coil. fMRI data was acquired using an echo-planar-imaging
331 (EPI) sequence with partial brain coverage: 36 sagittal slices were centred on the postcentral
332 gyrus with coverage over the thalamus and brainstem. We used the following parameters:
333 2.3mm$^3$ spatial resolution, TR: 2200ms, TE: 30ms, flip angle: 82˚, SENSE factor: 2.1, 36 slices.
334 We acquired 127 and 167 volumes for the finger and face stimulation runs,
335 respectively. Anatomical T1-weighted images for participants 1-9 were acquired using the
336 following acquisition parameters: TR = 7.7 ms, TE = 3.6 ms, flip angle = 8°, voxel size = 1

337 mm isotropic, transversal slices = 160. Anatomical T1-weighted images for participants 10-17
338 were acquired using the following acquisition parameters: 0.7mm$^3$ spatial resolution, TR:
339 9.3ms, TE: 4.4ms, flip angle: 8˚.
340
341 **MRI analysis**
342 fMRI analysis was implemented using tools from FSL v6.0
343 (https://fsl.fmrib.ox.ac.uk/fsl/fslwiki) in combination with the RSA toolbox (Nili et al., 2014;
344 Wesselink and Maimon-Mor, 2017) and in-house scripts developed using Matlab (R2018a).
345 Cortical surface analysis and visualisations were realised using Freesurfer
346 (https://surfer.nmr.mgh.harvard.edu/; Dale et al., 1999; Fischl et al., 2001).
347
348 ***Preprocessing and image coregistration***
349 Common preprocessing steps were applied to each individual fMRI run using FSL's Expert
350 Analysis Tool FEAT (version 6.0; https://fsl.fmrib.ox.ac.uk/fsl/fslwiki/FEAT). The following
351 preprocessing steps were included: motion correction using MCFLIRT (Jenkinson et al., 2002),
352 brain extraction using automated brain extraction tool BET (Smith, 2002), spatial smoothing
353 using a 2.3mm full-width-at-half-maximum (FWHM) Gaussian kernel, and high-pass temporal
354 filtering using a cut-off of 90s.
355 Image coregistration was done in separate, visually inspected, steps. For each
356 participant, a midspace (i.e., an average space in which images are minimally reoriented) was
357 calculated between the 4 face stimulation blocked design runs and, if the fingers were also
358 tested, between the four finger stimulation blocked design runs. We then transformed all fMRI
359 data to these functional midspaces using purely rigid probability mapping in ANTs. Next, we
360 registered each participant's midspace to the T1-weighted image, initially using 7 degrees of
361 freedom and the mutual information cost function, and then optimised using boundary based

362 registration (BBR; Greve and Fischl, 2009). Each coregistration step was visually inspected
363 and, if needed, manually optimised using blink comparison in Freeview. Structural images
364 were transformed to Montreal Neurological Institute (MNI) standard space using nonlinear
365 registration (FNIRT).
366
367 ***Univariate analysis***
368 First-level parameter estimates were computed using a voxel-based general linear model
369 (GLM) based on the gamma hemodynamic response function and its temporal derivatives.
370 Time series statistical analysis was carried out using FILM (FMRIB's Improved Linear Model)
371 with local autocorrelation correction. To reduce noise artifacts, CSF and WM scan wise time
372 series were added to the model as nuisance regressors. Data were further assessed for excessive
373 motion, and volumes with an estimated absolute mean displacement > 1.15mm (half of the
374 functional voxel size) were scrubbed. Contrasts were defined for each stimulation condition
375 versus rest, for overall face or finger stimulation conditions versus rest, and for each stimulation
376 condition versus all other stimulation conditions. We then used a fixed effects higher-level
377 analysis to average across the finger stimulation runs and across the face stimulation runs
378 separately for each individual participant. Z-statistic images were thresholded using clusters
379 determined by $Z > 2.3$ and $p < .05$ family-wise-error-corrected cluster significance thresholding
380 was applied.
381 To visualise inter-participant consistency of somatotopic finger and face selective
382 representations, we calculated cortical activation probability maps. Cortical surface projections
383 were constructed from participant's T1-weighted images. Each participant's cortical surface
384 was inflated into a sphere and aligned to the Freesurfer 2D average atlas using sulcal depth and
385 curvature information. The thresholded stimulation site selective (i.e., condition versus all
386 other stimulation conditions) contrast maps from each participant's fixed effects higher-level

387 analysis were resampled to the Freesurfer 2D average atlas and binarised. We then calculated
388 finger-specific and face part specific inter-participant probability maps.
389 Lastly, to visualise which brain areas were activated during overall face and fingers
390 stimulation, whole-brain group averages were assessed for the stimulation of all fingers versus
391 rest and stimulation of all face locations versus rest contrasts. Group-level analysis was
392 performed for the finger and face stimulations runs separately using FMRIB's Local Analysis
393 of Fixed and Mixed Effects (Woolrich et al., 2004), respectively. Data collected for individuals
394 of whom we tested the right side of the face was flipped on the midsagittal plane before
395 conducted group analysis to ensure that the tested hemisphere was consistently aligned. Z-
396 statistic images were thresholded using clusters determined by $Z > 3.1$ and $p < .05$ family-wise-
397 error-corrected cluster significance thresholding was applied. To visualise the group average
398 activity maps, statistical parametric activity maps were projected to the Freesurfer 2D average
399 atlas brain.
400
401 ***Representational similarity analysis***
402 A fuller description of somatotopic representations can be obtained by taking into account the
403 entire fine-grained activity pattern of stimulated finger or face parts. Representational
404 dissimilarity was therefore estimated between fingers or between face locations using the cross-
405 validated squared Mahalanobis distance (or crossnobis distance; Nili et al., 2014; Wesselink
406 and Maimon-Mor, 2017b). We closely followed previously described procedures (Kikkert et
407 al., 2021; Wesselink et al., 2019).
408 We first defined an anatomical S1 hand and an S1 face ROI using the probabilistic
409 Brodmann area parcellation provided by recon-all in Freesurfer. Each participant's cortical
410 parcellations for Brodmann areas 1, 2, 3a and 3b were converted to volumetric space and
411 merged to form a single S1 mask. Next, any holes in these converted masks were filled and the

412 non-zero voxels in the mask were mean dilated. We restricted this S1 mask such that it spanned
413 a 2cm strip medial/lateral to the anatomical location of the hand knob to form the S1 hand ROI
414 (Yousry et al., 1997). The S1 area inferior to this S1 hand ROI was then extracted to form the
415 S1 face ROI.

416 We computed the dissimilarity between the activity patterns measured for each pair of
417 stimulation conditions within the S1 hand or S1 face ROI for the fingers and face stimulation
418 runs, respectively. We extracted the voxel-wise parameter estimates (betas) and the model fit
419 residuals under the ROI and prewhitened the betas using the model fit residuals. We then
420 calculated the cross-validated squared Mahalanobis distances between each pair of conditions,
421 using the four runs as independent crossvalidation folds, and averaged the resulting distances
422 across the folds.

423 The dissimilarity values for all pairs of conditions were initially assembled in a
424 representational dissimilarity matrix (RDM), with a width and height corresponding to the
425 number of conditions (i.e., a 5x5 RDM for the finger stimulation runs and a 4x4 RDM for the
426 face stimulation runs). Since the RDM is mirrored across the diagonal with meaningless 0's on
427 the diagonal, all statistical analysis was conducted on the unique values of the RDM (10 unique
428 values for the finger stimulation runs and 6 unique values for the face stimulation runs). Finally,
429 we performed multidimensional scaling (MDS) to visualise the dissimilarity structure of the
430 RDM in an intuitive manner. MDS projects the higher-dimensional RDM into a lower-
431 dimensional space, while preserving the inter-condition dissimilarity values as well as possible
432 (Borg and Groenen, 2005). MDS was performed for each individual participant and then
433 averaged per group after Procrustes alignment to remove arbitrary rotation induced by MDS.

434 We estimated the strength of the representation or "representational separability" by
435 averaging the unique off-diagonal values of the RDM. If it is impossible to statistically
436 differentiate between conditions (i.e., when a parameter is not represented in the ROI), the

expected value of the distance estimate would be 0. If it is possible to distinguish between activity patterns this value will be larger than 0. To further ensure that our S1 face ROIs contained face information, we created a cerebral spinal fluid (CSF) ROI that would not contain somatotopic face information. We then repeated our face RSA analysis in this ROI and statistically compared the separability of the CSF ROI to the separability in the S1 face ROI.

**Statistics**

Statistical analysis was carried out using SPSS (v25). Non-parametric statistical testing was used for analysis of the finger stimulation data. Parametric statistical analysis was carried out for the face stimulation data after checking for normality using the Shapiro-wilk test. Non-parametric statistical testing in case of normality violations. All testing was two-tailed and we used the Benjamini-Hochberg procedure to control the false discovery rate with $q < 0.05$.

**Data availability**

Full details of the experimental protocol are available on clinicaltrials.gov under the number NCT03772548. Data is shared on <link will be made available upon publication>.

454 ## Results

455 In the current study, we aimed to validate the use of our newly developed SPA-setup for
456 somatotopic mapping using fMRI, we first explored whether SPA tactile stimulation would
457 elicit characteristic finger representations in S1. Next, we used our SPA setup to uncover the
458 somatotopic layout of the face in S1.

459

460 **Vibrotactile SPA stimulation induces activity in somatosensory processing areas**

461 We first examined activity elicited by tactile stimulation applied on the fingers (Figure 3A) and
462 on the face (Figure 3B) using our SPA setup. As expected, we found that both stimulation on
463 the fingers and on the face activated S1 and secondary somatosensory cortex (S2) contralateral
464 to the stimulation site. Ipsilateral S1 and S2 activity was less widespread for both the fingers
465 and face stimulation. Note that a direct comparison with regards to level of activity between
466 the finger and face stimulation runs is not accurate here given that activity elicited by fingers
467 stimulation was only tested on a subset of 8 participants and fixed effects modelling was used
468 to create the group activity map in Figure 3A. In contrast, 17 participants were tested to
469 examine activity elicited by face stimulation and mixed effects modelling was used to create
470 the group activity map in Figure 3B. Importantly, following the classical layout of the
471 homunculus (Penfield and Rasmussen, 1950), fingers stimulation activity was superior to the
472 face stimulation activity in S1.

473

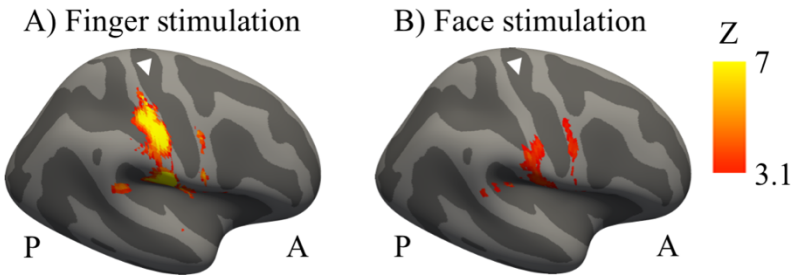


**Figure 3: Brain activity in the contralateral hemisphere during sensory stimulation using SPA technology.** Both fingers (A) and face (B) stimulation elicited activity in S1 and secondary somatosensory cortex. Consistent with previous reports and the classical layout of the homunculus, face stimulation elicited activity inferior to the hand representation. White arrows indicate the central sulcus. P = posterior, A = anterior.

## Finger representations

We hypothesized that if our SPA technology is reliable is mapping somatotopic representations, then we should observe typical finger somatotopy in the S1 hand area. Since the S1 hand representation contains a characteristic layout of finger selective representations that is relatively consistent across individuals, we first explored finger selective representations. We contrasted activity elicited during each finger stimulation against activity during stimulation of all other fingers and binarized the resulting finger selective maps. We then created inter-participant probability maps representing the number of participants exhibiting specific finger selectivity (i.e., using a winner-take-all approach) for each vertex in S1. These maps exhibited, as expected, that finger selectivity was not perfectly consistent across participants (Figure 4A; Kolasinski et al., 2016). Indeed, a given vertex was found to have finger selectivity selective for different fingers across participants. We did however observe a characteristic gradient of finger preference progressing from the thumb, for which inter-subject probability was highest lateral of the S1 hand area, to the little finger, for which inter-subject probability was highest medial of the S1 hand area. Qualitative inspection

suggests that inter-participant consistency was highest for the thumb and lowest for the little finger representation.

Next, we explored a 2nd somatotopic principle that is known to be consistent across individuals: the pattern of overlap between finger representations. We examined this intricate relationship between finger representations using representational similarity analysis. We found a typical pattern of inter-finger representational distances where neighbouring fingers have relatively lower representational distances compared to fingers that are further apart. Furthermore, fingers that we use more frequently together in daily life (e.g., the ring and little fingers) had lower representational distances compared to fingers we use more separately in daily life (e.g., the thumb and index fingers (Ejaz et al., 2015)). This inter-finger representational distance pattern found using SPA tactile stimulation of fingers (Figure 4B) was highly similar to the inter-finger representational distance patterns that we and others have described previously in fMRI experiments using individual finger movements (Ejaz et al., 2015; Kikkert et al., 2021, 2016; Sanders et al., 2019; Wesselink et al., 2019) or individual finger tactile stimulation (Sanders et al., 2019). The inter-finger representational distances were averaged across finger pairs within each participant to obtain an estimate for average inter-finger representational separability (see Figure 5C), or 'representation strength'. We found that inter-finger separability in the S1 hand area was greater than 0 ($Z = -2.52$, $p = 0.01$), showing that the S1 hand area contained information about individual finger representations. Furthermore, there was significant greater separability in the S1 hand area compared to a control cerebral spinal fluid (CSF) ROI that would not be expected to contain finger specific information ($Z = -2.52$, $p = 0.01$). Together, our results demonstrate that our SPA setup can be used to reliably map the well characterised somatotopic layout of the hand.

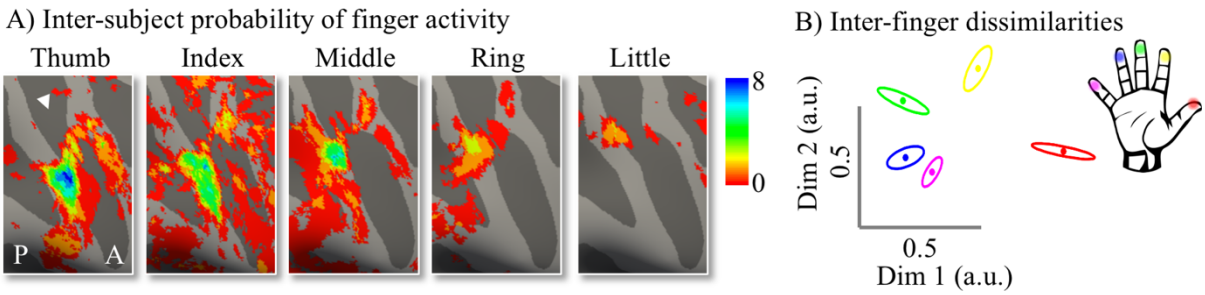


**Figure 4: SPA stimulation uncovers typical finger somatotopy.** A) inter-participant probability maps of finger selective representations. Colours indicate the number of participants (ranging from 1 (red) till 8 (blue)) who demonstrated finger selectivity for a given vertex. Typical finger selectivity is characterised by a progression of finger selectivity from the thumb (laterally) to the little finger (medially). We observed a characteristic gradient of finger preference progressing from the thumb, for which inter-subject probability was highest lateral of the S1 hand area, to the little finger, for which inter-subject probability was highest medial of the S1 hand area. Qualitative inspection suggests that inter-participant consistency was lowest for the little finger representation and highest for the thumb representation. The white arrow indicates the central sulcus. A = anterior; P = posterior. B) Two-dimensional projection of the representational structure of inter-finger distances. Inter-finger distance is reflected by the distance in the two dimensions. Individual fingers are represented by different colours: thumb = red; index finger = yellow; middle finger = green; ring finger = blue; little finger = purple. By stimulating fingers using SPA technology, we found a classical and frequently reported inter-finger distance pattern in the hand area of S1. Ellipses represent the between-participants standard error after Procrustes alignment.

## Face representations

One advantage of our SPA setup is that, unlike most commercially available vibrotactile devices, it is able to provide vibrotactile stimulation to localised areas of the face (i.e., in the MRI head coil) without causing any imaging artefacts or safety issues. We made use of this advantage by examining the somatotopic layout of the face using our SPA setup. First, as for the fingers, we created inter-participant probability maps of forehead, lip, chin, and thumb selective representations (Figure 5A). The resulting inter-participant probability maps represent the number of participants exhibiting selectivity (i.e., using a winner-take-all principle) for a specific stimulation site for each vertex in S1. Qualitative inspection suggests

that the selective thumb and lip activity was more consistent across participants compared to the forehead and chin. Furthermore, stimulation site selective activity was more consistent across participants in the contralateral compared to the ipsilateral hemisphere.

We used RSA in the S1 face area to investigate representational distances between stimulation sites (i.e., between the forehead, lip, chin and thumb) that were stimulated during the face stimulation runs (Figure 5B). The averaged representational distances (i.e., separability) between face sites (i.e., excluding the face-thumb distances) were markedly lower compared to the representational distances found between fingers in the S1 hand area (Figure 5C; $Z = -2.52$, $p = 0.01$). However, we found a clear pattern of inter-face site representational distances in the S1 face area revealing that the forehead had the lowest representational distance from the thumb. The chin had more representational distance from the thumb than the forehead, and the lips was most distant from the thumb.

We found that inter-face site (i.e., excluding the face-thumb distances) separability in the S1 face area was greater than 0 (Figure 5C; $t_{(16)} = 5.84$, $p < 0.001$), indicating that the S1 face area contained information about face sites. Separability between face sites was not significantly greater than 0 in a CSF ROI ($t_{(16)} = -0.25$, $p = 0.81$). Furthermore, there was significant greater separability in the S1 face area than in a control CSF ROI ($t_{(16)} = -6.00$, $p < 0.001$).

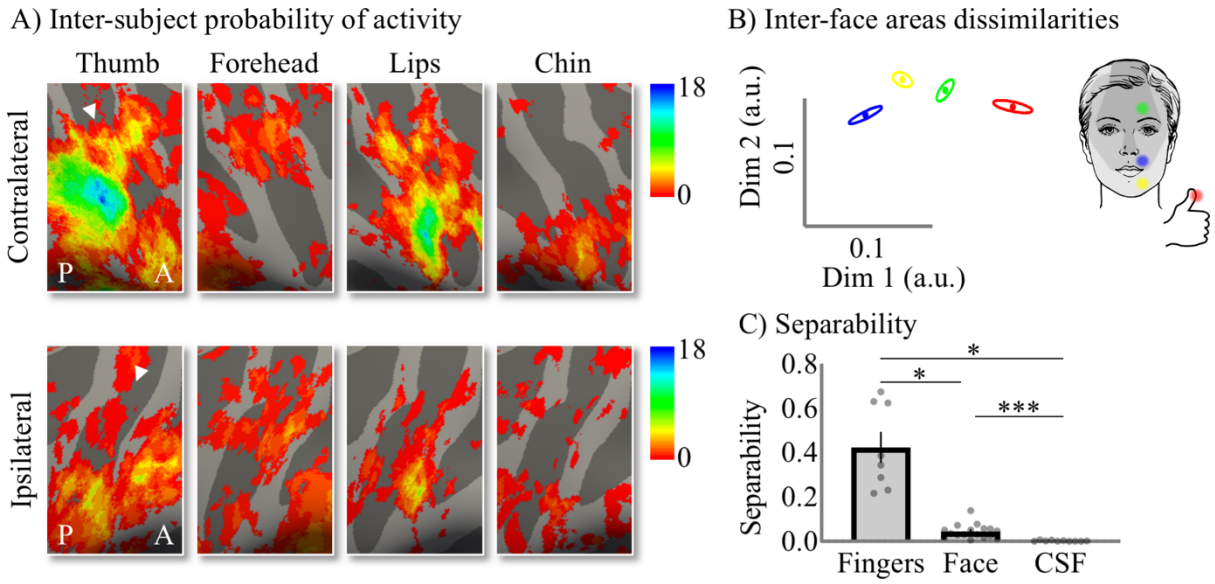


**Figure 5: Face somatotopy uncovered using SPA stimulation.** A) Inter-participant somatotopic probability face maps. Colours indicate the number of participants (ranging from 1 (red) till 17 (blue)) who demonstrated face part or thumb selectivity for a given vertex (i.e., stronger activity compared to the other stimulation sites). Qualitative inspection suggests that inter-participant consistency contralaterally was lowest for the forehead representation and highest for the thumb representation. Furthermore, inter-participant consistency was higher in contralateral, compared to ipsilateral S1. White arrows indicate the central sulcus. A = anterior; P = posterior. B) Two-dimensional projection of the representational structure of inter-stimulation site distances. Inter-stimulation site distance is reflected by the distance in the two dimensions. Individual stimulation sites are represented by different colours: thumb = red; chin = yellow; forehead = green; upper lip = blue. Ellipses represent the between-participants standard error after Procrustes alignment. C) Separability (i.e., average dissimilarity), or 'representation strength', for the fingers in the S1 hand area, for the face in the S1 face area, and for cerebral spinal fluid (calculated between face stimulation sites). There was significant separability (i.e., great than 0) for the fingers in the S1 hand area and for the face in the S1 face area. No significant separability was found in a control CSF ROI. Furthermore, separability for the fingers in the S1 hand area and for the face in the S1 face area was greater than separability in the control CSF ROI. Lastly, separability was higher for the fingers in the S1 hand area compared to separability in in the S1 face area. * = $p < 0.05$; *** = $p < 0.001$

580 **Discussion**

581 Providing somatosensory stimulation in an MR environment is challenging. Our results show
582 that somatosensory representations can be mapped using new SPA technology that is MR-
583 compatible and can be used within the MR head coil without causing artefacts. Using our SPA
584 setup, we found a typical somatotopic layout of participants' fingers, both in terms of the
585 gradient of finger selectivity and the inter-finger representational distance pattern. This
586 validates the use of our SPA setup for mapping somatotopic representations.

587 We further probed face somatotopy using automated tactile stimulation to the forehead,
588 lips, and chin – 3 face sites that are innervated by different branches of the trigeminal nerve.
589 Representational distances between the face sites were drastically reduced compared to the
590 representational distances between the fingers. Our face somatotopy results did not support a
591 clear inverted or straight-up representation of the face. Our univariate analysis revealed a great
592 degree of inter-participant variability of face-site selective representations. While the location
593 of the thumb and lip representations were relatively stable across participants, the forehead and
594 chin representations were much less stable. Potentially, the low density of mechanoreceptors
595 in the chin and forehead may have led to lower BOLD activations, causing them to be
596 'overshadowed' by the thumb and lip representations in this winner-take-all analysis. We
597 attempted to control for variability in sensed intensity using our intensity matching task.
598 Mechanoreceptor innervation in the skin of a given body part is suggested to be directly linked
599 to size of S1 representation (Catani, 2017; Penfield and Rasmussen, 1950). It is therefore likely
600 that the forehead and chin are represented less prominently in S1 compared to the thumb and
601 lip and may therefore not 'win' in winner-take-all univariate stimulation site selective analysis.
602 Indeed, we suggest that it is more appropriate in the study of face somatotopy to use an analysis
603 method that does not adhere to such a winner-take-all principle and instead is sensitive to
604 representational overlap or representational distances between face parts. Using RSA, we

605 revealed that the forehead was least distance to the thumb representation, followed by the chin
606 representation, and lastly by the lip representation. These results are in line with, and extend
607 the results of, a recent study using RSA and movements of the forehead, nose, lips, and tongue
608 to study face somatotopy in S1. As in our study, Root et al. (2021) reported that the forehead
609 neighboured the hand representation. They further found that the nose closely neighboured the
610 forehead representation and that the lips were furthest from the forehead representation. Root
611 et al. (2021) could not disentangle the lips and chin representation, due to the nature of their
612 movement task. As such, we extend their results by showing that the chin representation is in-
613 between the lip and forehead representation in S1.

614 The aim of this study was to construct a simple MR-compatible pneumatic vibrotactile
615 device for implementation in somatotopic mapping experiments. While pneumatic tactile
616 stimulators are highly applicable in studies investigating somatotopy, especially when
617 investigating body part representations in or nearby the MR head coil, they generally have a
618 smaller frequency range and more limited actuation control compared to piezoelectric devices.
619 Due to the length of our plastic tubes, our SPA setup can provide accurate control of
620 frequencies up to 35Hz. While this stimulation frequency is reasonable for somatotopic
621 mapping experiments, it may not be ideal when investigating neural responses to stimulation
622 of specific mechanoreceptors. Furthermore, while our SPA setup can stimulate suprathreshold,
623 its stimulation amplitude is limited due to the nature of the SPA material. As such, it is not
624 suitable for studies requiring highly intense sensations on skin surfaces with low innervation
625 of mechanoreceptors (e.g., on the neck or ankle). Furthermore, the pneumatic supply system
626 components (tubing resistance, compressibility and inertia of the oscillating air, conductance
627 of various components) and the extent of grounding force with which the SPA is fixed to the
628 stimulation site influences the exact amount of skin indentation. The overall control system is
629 optimized using the process presented in Joshi et al., (2021) for individual components.

Together our results show that, by providing vibrotactile stimulation using the SPA-technology, we are able to reveal clear somatotopic representational patterns of different body parts. Given that in our SPA-setup, all materials in the MRI scanner room are non-metallic, no MR safety and image quality certifications are required when using this device. SPAs are small and can easily be attached to different sites of the body. The SPA setup is flexible, easy-to-implement, precise, portable, fast and offers a cost-effective solution in comparison to commercially available devices that often induce artefacts, are highly expensive, require active shielding, or hardware modifications.

## Acknowledgements

We thank Lena Salzmann, Lydia Kampf, Nicolin Gauler, Philipp Barzyk, Silvia Hofer, Daniel Reichmuth, and Sijamini Baskaralingam for assistance with piloting or data collection. We thank Dan Woolley and Charles Lambelet for technical support. We thank Roger Lüchinger for assistance with artefact testing.

## Funding

This study was funded by the Swiss National Science Foundation (SNF 320030_175616). SK is supported by the ETH Zurich Postdoctoral Fellowship Program. PF is funded by a SNF Eccellenza Professorial Fellowship grant (PCEFP3_181362 / 1). NW is supported by the Swiss National Science Foundation (SNF 320030_175616). HS and JP are supported by the Swiss National Science Foundation and École polytechnique fédérale de Lausanne.

## Competing interests

The authors declare that no current competing interests exist.

## References

Agarwal, G., Robertson, M.A., Sonar, H., Paik, J., 2017. Design and Computational Modeling of a Modular, Compliant Robotic Assembly for Human Lumbar Unit and Spinal Cord Assistance. Sci. Rep. 7, 14391. https://doi.org/10.1038/s41598-017-14220-3

Alahakone, A.U., Senanayake, S.M.N.A., 2009. Vibrotactile feedback systems: Current trends in rehabilitation, sports and information display, in: 2009 IEEE/ASME International Conference on Advanced Intelligent Mechatronics. IEEE, pp. 1148–1153. https://doi.org/10.1109/AIM.2009.5229741

Bauer, S., Bauer-Gogonea, S., Graz, I., Kaltenbrunner, M., Keplinger, C., Schwödiauer, R., 2014. 25th anniversary article: A soft future: From robots and sensor skin to energy harvesters. Adv. Mater. 26, 149–162. https://doi.org/10.1002/adma.201303349

Borg, I., Groenen, P.J.F., 2005. Modern multidimensional scaling: Theory and applications, 2nd ed., Modern multidimensional scaling: Theory and applications, 2nd ed.

Catani, M., 2017. A little man of some importance. Brain 140, 3055–3061. https://doi.org/10.1093/brain/awx270

Chen, C. fu, Kreutz-Delgado, K., Sereno, M.I., Huang, R.S., 2017. Validation of periodic fMRI signals in response to wearable tactile stimulation. Neuroimage 150, 99–111. https://doi.org/10.1016/j.neuroimage.2017.02.024

Cholewiak, R.W., Collins, A.A., 2003. Vibrotactile localization on the arm: Effects of place, space, and age. Percept. Psychophys. 65, 1058–1077. https://doi.org/10.3758/BF03194834

Corbetta, M., Burton, H., Sinclair, R.J., Conturo, T.E., Akbudak, E., McDonald, J.W., 2002. Functional reorganization and stability of somatosensory-motor cortical topography in a tetraplegic subject with late recovery. Proc. Natl. Acad. Sci. U. S. A. 99, 17066–17071. https://doi.org/10.1073/pnas.262669099

Corniani, G., Saal, H.P., 2020. Tactile innervation densities across the whole body. J. Neurophysiol. 124, 1229–1240. https://doi.org/10.1152/jn.00313.2020

Custead, R., Oh, H., Wang, Y., Barlow, S., 2017. Brain encoding of saltatory velocity through a pulsed pneumotactile array in the lower face. Brain Res. 1677, 58–73. https://doi.org/10.1016/j.brainres.2017.09.025

Dale, A.M., Fischl, B., Sereno, M.I., 1999. Cortical surface-based analysis. Neuroimage 9, 179–194. https://doi.org/10.1006/nimg.1998.0395

DaSilva, A.F., Becerra, L., Makris, N., Strassman, A.M., Gonzalez, R.G., Geatrakis, N.,

Borsook, D., 2002. Somatotopic activation in the human trigeminal pain pathway. J Neurosci 22, 8183–8192. https://doi.org/22/18/8183 [pii]

Dresel, C., Parzinger, A., Rimpau, C., Zimmer, C., Ceballos-Baumann, A.O., Haslinger, B., 2008. A new device for tactile stimulation during fMRI. Neuroimage 39, 1094–1103. https://doi.org/10.1016/j.neuroimage.2007.09.033

Ejaz, N., Hamada, M., Diedrichsen, J., 2015. Hand use predicts the structure of representations in sensorimotor cortex. Nat. Neurosci. 18, 1034–1040.

Fischl, B., Liu, A., Dale, A.M., 2001. Automated manifold surgery: Constructing geometrically accurate and topologically correct models of the human cerebral cortex. IEEE Trans. Med. Imaging 20, 70–80. https://doi.org/10.1109/42.906426

Flor, H., Elbert, T., Knecht, S., Wienbruch, C., Pantev, C., Birbaumer, N., Larbig, W., Taub, E., 1995. Phantom-limb pain as a perceptual correlate of cortical reorganization following arm amputation. Nature 375, 482–484.

Gallasch, E., Fend, M., Rafolt, D., Nardone, R., Kunz, A., Kronbichler, M., Beisteiner, R., Golaszewski, S., 2010. Cuff-type pneumatic stimulator for studying somatosensory evoked responses with fMRI. Neuroimage 50, 1067–1073. https://doi.org/10.1016/j.neuroimage.2010.01.014

Gibson, R., 2018. Wearable Technologies in Academic Information Search, in: Wearable Technologies: Concepts, Methodologies, Tools, and Applications. IGI Global, pp. 665–688.

Golaszewski, S.M., Zschiegner, F., Siedentopf, C.M., Unterrainer, J., Sweeney, R.A., Eisner, W., Lechner-steinleitner, S., Mottaghy, F.M., Felber, S., 2002. A new pneumatic vibrator for functional magnetic resonance imaging of the human sensorimotor cortex. Neurosci. Lett. 324, 1–4.

Greve, D.N., Fischl, B., 2009. Accurate and robust brain image alignment using boundary-

based registration. Neuroimage 48, 63–72. https://doi.org/10.1016/j.neuroimage.2009.06.060

Hawkes, E.W., Blumenschein, L.H., Greer, J.D., Okamura, A.M., 2017. A soft robot that navigates its environment through growth. Sci. Robot. 2, 1–8. https://doi.org/10.1126/scirobotics.aan3028

Huang, R.-S., Chen, C., Sereno, M.I., 2017. Mapping the complex topological organization of the human parietal face area. Neuroimage 1–12. https://doi.org/10.1016/j.neuroimage.2017.09.004

Huang, R.S., Sereno, M.I., 2007. Dodecapus: An MR-compatible system for somatosensory stimulation. Neuroimage 34, 1060–1073. https://doi.org/10.1016/j.neuroimage.2006.10.024

Jafari, N., Adams, K.D., Tavakoli, M., 2016. Haptics to improve task performance in people with disabilities: A review of previous studies and a guide to future research with children with disabilities. J. Rehabil. Assist. Technol. Eng. 3, 205566831666814. https://doi.org/10.1177/2055668316668147

Jenkinson, M., Bannister, P., Brady, M., Smith, S.M., 2002. Improved optimization for the robust and accurate linear registration and motion correction of brain images. Neuroimage 17, 825–841. https://doi.org/10.1016/S1053-8119(02)91132-8

Jones, L.A., 2011. Tactile communication systems: optimizing the display of information, in: Progress in Brain Research. Elsevier, pp. 113–128. https://doi.org/doi: 10.1016/B978-0-444-53355-5.00008-7

Joshi, S., Paik, J., 2021. Pneumatic Supply System Parameter Optimization for Soft Actuators. Soft Robot. 8, 152–163. https://doi.org/10.1089/soro.2019.0134

Joshi, S., Sonar, H., Paik, J., 2021. Flow path optimization for soft pneumatic actuators: Towards optimal performance and portability. IEEE Robot. Autom. Lett. 6, 7949–7956.

https://doi.org/10.1109/LRA.2021.3100626

Jutzeler, C.R., Curt, A., Kramer, J.L.K., 2015. Relationship between chronic pain and brain reorganization after deafferentation: A systematic review of functional MRI findings. NeuroImage Clin. 9, 599–606. https://doi.org/10.1016/j.nicl.2015.09.018

Kikkert, S., Kolasinski, J., Jbabdi, S., Tracey, I., Beckmann, C.F., Johansen-Berg, H., Makin, T.R., 2016. Revealing the neural fingerprints of a missing hand. Elife 5, e15292. https://doi.org/10.7554/eLife.15292

Kikkert, S., Pfyffer, D., Verling, M., Freund, P., Wenderoth, N., 2021. Finger somatotopy is preserved after tetraplegia but deteriorates over time. Elife. https://doi.org/10.7554/eLife.67713

Kolasinski, J., Makin, T.R., Jbabdi, S., Clare, S., Stagg, C.J., Johansen-Berg, H., 2016. Investigating the stability of fine-grain digit somatotopy in individual human participants. J. Neurosci. 36, 1113–1127.

Makin, T.R., Scholz, J., Henderson Slater, D., Johansen-Berg, H., Tracey, I., 2015. Reassessing cortical reorganization in the primary sensorimotor cortex following arm amputation. Brain 138, 2140–2146. https://doi.org/10.1093/brain/awv161

Martuzzi, R., Zwaag, W. Van Der, Farthouat, J., Gruetter, R., Blanke, O., 2014. Human Finger Somatotopy in Areas 3b , 1 , and 2 : A 7T fMRI Study Using A Natural Stimulus 226, 213–226. https://doi.org/10.1002/hbm.22172

Moseley, P., Florez, J.M., Sonar, H.A., Agarwal, G., Curtin, W., Paik, J., 2016. Modeling, Design, and Development of Soft Pneumatic Actuators with Finite Element Method. Adv. Eng. Mater. 18, 978–988. https://doi.org/10.1002/adem.201500503

Moulton, E.A., Pendse, G., Morris, S., Aiello-Lammens, M., Becerra, L., Borsook, D., 2009. Segmentally arranged somatotopy within the face representation of human primary somatosensory cortex. Hum. Brain Mapp. 30, 757–765.

https://doi.org/10.1002/hbm.20541

Moxon, K.A., Oliviero, A., Aguilar, J., Foffani, G., 2014. Cortical reorganization after spinal cord injury: Always for good? Neuroscience 283, 78–94. https://doi.org/10.1016/j.neuroscience.2014.06.056

Nili, H., Wingfield, C., Walther, A., Su, L., Marslen-Wilson, W., Kriegeskorte, N., 2014. A Toolbox for Representational Similarity Analysis. PLoS Comput. Biol. 10. https://doi.org/10.1371/journal.pcbi.1003553

Penfield, W., Rasmussen, T., 1950. The Cerebral Cortex of Man. A Clinical Study of Localization of Function.pdf. Acad. Med. https://doi.org/10.1097/00001888-195009000-00037

Polygerinos, P., Correll, N., Morin, S.A., Mosadegh, B., Onal, C.D., Petersen, K., Cianchetti, M., Tolley, M.T., Shepherd, R.F., 2017. Soft Robotics: Review of Fluid-Driven Intrinsically Soft Devices; Manufacturing, Sensing, Control, and Applications in Human-Robot Interaction. Adv. Eng. Mater. 19. https://doi.org/10.1002/adem.201700016

Polygerinos, P., Wang, Z., Galloway, K.C., Wood, R.J., Walsh, C.J., 2015. Soft robotic glove for combined assistance and at-home rehabilitation. Rob. Auton. Syst. 73, 135–143. https://doi.org/10.1016/j.robot.2014.08.014

Pons, J.L., 2008. Wearable robots: biomechatronic exoskeletons. John Wiley & Sons, Ltd.

Puckett, A.M., Bollmann, S., Barth, M., Cunnington, R., 2017. Measuring the effects of attention to individual fingertips in somatosensory cortex using ultra-high field (7T) fMRI. Neuroimage 161, 179–187. https://doi.org/10.1016/j.neuroimage.2017.08.014

Robertson, M.A., Paik, J., 2017. New soft robots really suck: Vacuum-powered systems empower diverse capabilities. Sci. Robot. 2, 1–12. https://doi.org/10.1126/scirobotics.aan6357

Root, V., Muret, D., Arribas, M., Amoruso, E., Thornton, J., 2021. Investigating facial information content in the hand area of individuals with a congenital and acquired missing hand. bioRxiv.

Roux, F.E., Djidjeli, I., Durand, J.B., 2018. Functional architecture of the somatosensory homunculus detected by electrostimulation. J. Physiol. 596, 941–956. https://doi.org/10.1113/JP275243

Sanchez-Panchuelo, R.M., Francis, S., Bowtell, R., Schluppeck, D., 2010. Mapping human somatosensory cortex in individual subjects with 7T functional MRI. J. Neurophysiol. 103, 2544–2556. https://doi.org/10.1152/jn.01017.2009

Sanders, Z.-B., Wesselink, D.B., Dempsey-Jones, H., Makin, T.R., 2019. Similar somatotopy for active and passive digit representation in primary somatosensory cortex. bioRxiv 1–36. https://doi.org/10.1101/754648

Sato, K., Nariai, T., Tanaka, Y., Maehara, T., Miyakawa, N., Sasaki, S., Momose-Sato, Y., Ohno, K., 2005. Functional representation of the finger and face in the human somatosensory cortex: Intraoperative intrinsic optical imaging. Neuroimage 25, 1292–1301. https://doi.org/10.1016/j.neuroimage.2004.12.049

Schellekens, W., Petridou, N., Ramsey, N.F., 2018. NeuroImage Detailed somatotopy in primary motor and somatosensory cortex revealed by Gaussian population receptive fi elds. Neuroimage 179, 337–347. https://doi.org/10.1016/j.neuroimage.2018.06.062

Schwartz, T.H., Li, M.C., Friedman, R.M., Spencer, D.D., Roe, A.W., 2004. Intraoperative optical imaging of human face cortical topography: A case study. Neuroreport 15, 1527–1531. https://doi.org/10.1097/01.wnr.0000131006.59315.2f

Servos, P., Engel, S. a, Gati, J., Menon, R., 1999. fMRI evidence for an inverted face representation in human somatosensory cortex. Neuroreport 10, 1393–5. https://doi.org/10.1097/00001756-199905140-00002

Smart Tactor Development Kit [WWW Document], 2021. . https://piezo.com/products/haptic-piezo-actuator-development-kit-1.

Smith, S.M., 2002. Fast robust automated brain extraction. Hum. Brain Mapp. 17, 143–155. https://doi.org/10.1002/hbm.10062

Sonar, Harshal A., Gerratt, A.P., Lacour, S.P., Paik, J., 2019. Closed-Loop Haptic Feedback Control Using a Self-Sensing Soft Pneumatic Actuator Skin. Soft Robot. 00, 1–8. https://doi.org/10.1089/soro.2019.0013

Sonar, H.A., Paik, J., 2016. Soft pneumatic actuator skin with piezoelectric sensors for vibrotactile feedback. Front. Robot. AI 2, 38. https://doi.org/10.3389/frobt.2015.00038

Sonar, H A, Robertson, M.A., Joshi, S.D., Bhatnagar, T., Paik, J., 2019. A soft portable wearable pneumatic interactive suit. WO2018220596A3.

Sonar, H.A., Yuen, M.C., Kramer-Bottiglio, R., Paik, J., 2018. An any-resolution pressure localization scheme using a soft capacitive sensor skin, in: 2018 IEEE International Conference on Soft Robotics (RoboSoft). IEEE, pp. 170–175. https://doi.org/10.1109/ROBOSOFT.2018.8404915

Van Der Zwaag, W., Gruetter, R., Martuzzi, R., 2015. Stroking or buzzing? a comparison of somatosensory touch stimuli using 7 tesla fMRI. PLoS One 10, 1–15. https://doi.org/10.1371/journal.pone.0134610

Wesselink, D.B., Maimon-Mor, R., 2017. Github [WWW Document].

Wesselink, D.B., van den Heiligenberg, F.M., Ejaz, N., Dempsey-Jones, H., Cardinali, L., Tarall-Jozwiak, A., Diedrichsen, J., Makin, T.R., 2019. Obtaining and maintaining cortical hand representation as evidenced from acquired and congenital handlessness. Elife 8, 1–19. https://doi.org/10.7554/elife.37227

Woolrich, M.W., Behrens, T.E.J., Beckmann, C.F., Jenkinson, M., Smith, S.M., 2004. Multilevel linear modelling for FMRI group analysis using Bayesian inference.

Neuroimage 21, 1732–1747. https://doi.org/10.1016/j.neuroimage.2003.12.023

Yang, T.T., Gallen, C.C., Schwartz, B.J., Bloom, F.E., 1993. Noninvasive somatosensory homunculus mapping in humans by using a large-array biomagnetometer. Neurobiology 90, 3098–3102. https://doi.org/10.1073/pnas.90.7.3098

Yousry, T.A., Schmid, U.D., Alkadhi, H., Schmidt, D., Peraud, A., Buettner, A., Winkler, P., 1997. Localization of the motor hand area to a knob on the precentral gyrus. A new landmark. Brain 120, 141–157. https://doi.org/10.1093/brain/120.1.141

Yu, N., Riener, R., 2006. Review on MR-compatible robotic systems. Proc. First IEEE/RAS-EMBS Int. Conf. Biomed. Robot. Biomechatronics, 2006, BioRob 2006 2006, 661–665. https://doi.org/10.1109/BIOROB.2006.1639165

Yun, S.-S., Kang, B.B., Cho, K.-J., 2017. Exo-Glove PM: An Easily Customizable Modularized Pneumatic Assistive Glove. IEEE Robot. Autom. Lett. 2, 1725–1732. https://doi.org/10.1109/LRA.2017.2678545

Zeharia, N., Hertz, U., Flash, T., Amedi, A., 2015. New whole-body sensory-motor gradients revealed using phase-locked analysis and verified using multivoxel pattern analysis and functional connectivity. J. Neurosci. 35, 2845–2859. https://doi.org/10.1523/Jneurosci.4246-14.2015